Experimental and theoretical study of rotationally inelastic diffraction of H2(D2) from methyl-terminated Si(111)

Kevin J. Nihill, Zachary M. Hund, Alberto Muzas, Cristina Díaz, Marcos del Cueto, Terry Frankcombe, Noah T. Plymale, Nathan S. Lewis, Fernando Martín, and S. J. Sibener

Articles you may be interested in

Vibrational dynamics and band structure of methyl-terminated Ge(111)
J. Chem. Phys. 143, 124705 (2015); 10.1063/1.4931178

Differential and integral cross sections for the rotationally inelastic scattering of methyl radicals with H2 and D2
J. Chem. Phys. 140, 204318 (2014); 10.1063/1.4879618

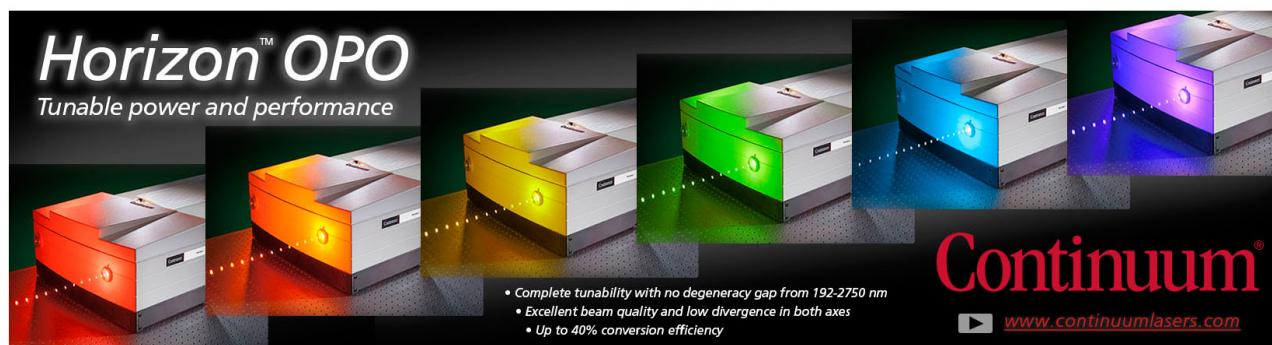Guided ion beam and theoretical study of the reactions of Os+ with H2, D2, and HD
J. Chem. Phys. 135, 234302 (2011); 10.1063/1.3669425

Rotational effects in dissociation of H 2 on Pd(111): Quantum and classical study
J. Chem. Phys. 119, 12553 (2003); 10.1063/1.1626535

Reactive and diffractive scattering of H 2 from Pt(111) studied using a six-dimensional wave packet method
J. Chem. Phys. 117, 5885 (2002); 10.1063/1.1501121

Experimental and theoretical study of rotationally inelastic diffraction of H₂(D₂) from methyl-terminated Si(111)

Kevin J. Nihill,[1,a)] Zachary M. Hund,[1,a)] Alberto Muzas,[2] Cristina Díaz,[2,3] Marcos del Cueto,[2] Terry Frankcombe,[4] Noah T. Plymale,[5] Nathan S. Lewis,[5] Fernando Martín,[2,3,6] and S. J. Sibener[1,b)]

[1]*The James Franck Institute and Department of Chemistry, The University of Chicago, 929 E. 57th Street, Chicago, Illinois 60637, USA*
[2]*Departamento de Química, Módulo 13, Universidad Autónoma de Madrid, 28049 Madrid, Spain*
[3]*Condensed Matter Physics Center (IFIMAC), Universidad Autónoma de Madrid, 28049 Madrid, Spain*
[4]*School of Physical, Environmental and Mathematical Sciences, University of New South Wales, Canberra ACT 2610, Australia*
[5]*Division of Chemistry and Chemical Engineering, Beckman Institute and Kavli Nanoscience Institute, California Institute of Technology, 210 Noyes Laboratory, 127-72, Pasadena, California 91125, USA*
[6]*Instituto Madrileño de Estudios Avanzados en Nanociencia (IMDEA-Nanociencia), Cantoblanco, 28049 Madrid, Spain*

Fundamental details concerning the interaction between H₂ and CH₃–Si(111) have been elucidated by the combination of diffractive scattering experiments and electronic structure and scattering calculations. Rotationally inelastic diffraction (RID) of H₂ and D₂ from this model hydrocarbon-decorated semiconductor interface has been confirmed for the first time via both time-of-flight and diffraction measurements, with modest $j = 0 \rightarrow 2$ RID intensities for H₂ compared to the strong RID features observed for D₂ over a large range of kinematic scattering conditions along two high-symmetry azimuthal directions. The Debye-Waller model was applied to the thermal attenuation of diffraction peaks, allowing for precise determination of the RID probabilities by accounting for incoherent motion of the CH₃–Si(111) surface atoms. The probabilities of rotationally inelastic diffraction of H₂ and D₂ have been quantitatively evaluated as a function of beam energy and scattering angle, and have been compared with complementary electronic structure and scattering calculations to provide insight into the interaction potential between H₂ (D₂) and hence the surface charge density distribution. Specifically, a six-dimensional potential energy surface (PES), describing the electronic structure of the H₂(D₂)/CH₃−Si(111) system, has been computed based on interpolation of density functional theory energies. Quantum and classical dynamics simulations have allowed for an assessment of the accuracy of the PES, and subsequently for identification of the features of the PES that serve as classical turning points. A close scrutiny of the PES reveals the highly anisotropic character of the interaction potential at these turning points. This combination of experiment and theory provides new and important details about the interaction of H₂ with a hybrid organic-semiconductor interface, which can be used to further investigate energy flow in technologically relevant systems. *Published by AIP Publishing.* [http://dx.doi.org/10.1063/1.4961257]

I. INTRODUCTION

This study details the first rotationally inelastic diffraction (RID) of molecular hydrogen from a hybrid organic-semiconductor interface, bolstering the understanding of technologically relevant systems, such as fuel cells and biosensing electronics, where the interaction of H₂ with the surface charge density distribution of these materials is of paramount interest.[1–7] The nature of gas interactions at solid surfaces has been thoroughly examined through characterizations of chemisorption for a variety of interfaces, providing a strong basis for understanding the processes involved in surface chemical reactions.[8] While a traditional route for understanding molecular chemisorption is monitoring the fraction of molecules that stick to a given surface,[9] it has been theoretically demonstrated and experimentally proven that diffraction of molecules from a surface can provide complementary and precise information regarding the gas-surface interaction potential.[10,11] Diffraction patterns of diatomic molecules in particular have highlighted the role of rotational degrees of freedom in the chemisorption process, indicating a direct effect on dissociative probabilities and revealing fundamental details concerning the interaction of gases with surface charge densities.[8,12]

Methyl-terminated Si(111) features a complete (1 × 1) methyl termination of its underlying lattice, endowing this surface with improved interfacial electronic properties and surface passivation, and establishing it as a model system for the understanding of organic-functionalized

a)K. J. Nihill and Z. M. Hund contributed equally to this work.
b)Author to whom correspondence should be addressed. Electronic mail: s-sibener@uchicago.edu

systems. This interface has been thoroughly characterized by many experimental and theoretical techniques: the surface structure and extent of methyl termination have been surveyed by elastic helium atom scattering,[13–15] scanning tunneling microscopy,[16,17] and synchrotron-based x-ray photoelectron spectroscopy (XPS),[18] and the vibrational dynamics were studied via high-resolution electron energy loss spectroscopy,[19] transmission infrared spectroscopy,[20,21] and inelastic helium atom scattering in conjunction with density functional perturbation theory.[14,15] This study employs rotationally inelastic diffraction and accompanying scattering calculations to further explore the surface charge density of CH_3–Si(111) and probe the interaction potential with H_2, broadening the understanding of the anisotropic features of this system. This potential anisotropy can serve a fundamental role in dissociative chemisorption for thin-film systems.

Rotationally inelastic diffraction (RID), whereby diatomic molecules impinging upon a surface convert translational energy into rotational energy (or *vice versa*) and are scattered into unique angular channels, was first reported in experiments involving diffraction of H_2 from MgO and LiF in the 1930s.[22–24] Since then, this technique has seen improvements through gains in angular resolution that have allowed a more precise investigation of the RID peaks.[25,26] High angular resolution and a wide range of incident energies have enabled the widespread use of RID, with the goal of investigating the gas-surface potential for a variety of systems.[22,25,27–29] These studies have provided a wealth of information not only on the nature of interfacial dynamics but also on the theory that has been developed to study them.[22,23,30,31]

The dependence of diatomic diffraction on molecular orientation processes makes theoretical modeling of the interaction a distinctly more complicated task than for monatomic systems such as He,[32] because the rotational transitions that occur at the surface are highly sensitive not only to the anisotropy of the interactions but also to the corrugation of the gas-surface interaction potential and the coupling of these two factors.[23] However, a number of combined theoretical and experimental studies have already attempted to understand better the effect of parallel momentum transfer on elastic[33–35] and rotationally inelastic diffraction.[22,36] State-of-the-art theoretical models have shown some limitations, for example, in accurately reproducing the intensities of RID peaks relative to their elastic counterparts. However, they have proven very useful in reproducing general trends,[11,30,31,37,38] which are the result of the main features characterizing the underlying potential energy surfaces (PESs), such as the corrugation and the anisotropy.

This paper presents the first rotationally inelastic diffraction measurements on an organic-functionalized semiconductor. In contrast to the various metal and alloy surfaces that have been characterized via RID, CH_3–Si(111) represents a new soft-film, i.e., low Debye temperature system for experimental studies. High-resolution rotationally inelastic diffraction of H_2 and D_2 has been employed to study the anisotropy of the CH_3–Si(111) surface via comparison with quantum dynamics simulations. The low-energy molecular

diffraction measurements performed herein are primarily surface-sensitive, revealing information on the structure, charge density, and interfacial properties of the surface and its interactions with impinging molecules. This low incident energy permits a valid use of the rigid rotor assumption and energetically forbids vibrational excitations at the energies used.[32] Rotationally inelastic diffraction spectra for H_2 and D_2 are compared, demonstrating much greater rotational excitation probabilities for D_2. Measurements of experimental RID excitations relative to elastic scattering events are examined as a function of incident angle and beam energy. The precision of these rotational probabilities is improved by employing the Debye-Waller model to account for the attenuation of diffraction peak intensities as a function of increasing surface temperature. Experimentally measured RID probabilities indicate a greater likelihood, not unexpectedly, of rotational excitation for higher beam energies, but show no significant dependence on incident angle. The potential energy surface (PES) of the $H_2(D_2)$/CH_3–Si(111) system has been modeled by interpolation of a density functional theory (DFT) energies data set, and used to study rotationally inelastic scattering and to simulate RID probabilities by means of quasi-classical and quantum dynamics. Quantum dynamics simulations have been used to assess the accuracy of the PES through a direct comparison with experimental results, whereas quasi-classical trajectories have been used to track down the aspects of the molecule-surface PES that lead to rotational excitation. These classical turning points show both large corrugation and high anisotropy for the interaction, as revealed by a thorough survey of the polar angular dependence of the PES landscape on these regions.

II. METHODS

A. Methyl–Si sample preparation

All chemicals were used as received. Water ($\geq$18.2 MΩ cm) was obtained from a Barnstead Nanopure system. Czochralski-grown n-Si wafers (Virginia Semiconductor, Fredericksburg, VA), 381 $\pm$ 25 μm thick, were double-side polished, doped with phosphorus to a resistivity of 1 Ω cm, and oriented to within 0.1° of the (111) crystal plane. CH_3–Si(111) surfaces were prepared according to a published procedure.[39] The wafers were cut into 1 cm $\times$ 3 cm pieces and rinsed sequentially with water, methanol ($\geq$99.8%, EMD), acetone ($\geq$99.5%, BDH), methanol, and water. Organic contaminants were removed and the surfaces were oxidized by immersing the wafers in a freshly prepared piranha solution (1:3 v/v of 30% H_2O_2(aq) (EMD):18M H_2SO_4 (EMD)) at 90–95 °C for 10 min. The piranha solution was drained and the wafers were rinsed with copious amounts of water. Atomically flat H-terminated surfaces were prepared[40] by immersing the cleaned wafers in buffered HF(aq) (Transene Co., Inc., Danvers, MA) for 18 s, rinsing with water, and immediately placing the wafers in an Ar-purged solution of NH_4F(aq) (40%, Transene Co., Inc.) for 9 min. The wafers were agitated periodically to remove bubbles that formed on the surface. The Si samples were removed from the NH_4F(aq) solution, rinsed with water, and dried under a stream of N_2.

The Si wafers were chlorinated inside a N_2-purged glove box with <10 ppm O_2. A saturated solution of PCl_5 (99.998% metal basis, Alfa Aesar) in chlorobenzene (anhydrous, ≥99.8%, Sigma-Aldrich) was preheated with an initiating amount (<1 mg/ml) of benzoyl peroxide (≥98%, Sigma-Aldrich). The wafers were rinsed with chlorobenzene and reacted in the PCl_5 solution at 90 ± 2 °C for 45 min. The reaction solution was drained and the wafers were rinsed with copious amounts of chlorobenzene, followed by tetrahydrofuran (THF, anhydrous, inhibitor-free, ≥99.9%, Sigma-Aldrich).

The Cl-terminated surfaces were alkylated in a 1.0 M–3.0 M solution of CH_3MgCl (Sigma-Aldrich or Fisher Scientific) in THF. The reaction solution was heated to 50 ± 2 °C for >12 h. The reaction solution was drained and the wafers were rinsed with THF, submerged in THF, and removed from the N_2-purged glove box. The samples were sonicated sequentially for 10 min in each of THF, methanol, and water. The wafers were broken into 1 cm^2 pieces, dried under a stream of N_2, and sealed under Ar for shipment from Pasadena, CA to Chicago, IL. X-ray photoelectron spectroscopy (XPS) indicated that the surfaces were fully terminated with Si–C bonds and that there was no detectable surface oxidation.

B. H_2 and D_2 diffraction techniques

To measure the elastic and rotationally inelastic diffraction peaks, these experiments required the use of an energy- and momentum-resolved ultra-high vacuum (UHV) scattering apparatus. This instrument has been described in full detail elsewhere;[41] in brief, this apparatus consists of three primary sections: a differentially pumped beam-source manifold, an UHV crystal chamber, and a rotatable mass spectrometer detector. For beam generation, high pressures (800–2000 psi) of ultra-high purity gases (He, H_2, D_2) are expanded through a 15 μm diameter nozzle source that is cooled by a closed-cycle helium refrigerator to generate an intense and nearly monoenergetic ($\Delta v/v \leq 1$% for He, 10% for H_2, D_2) supersonic neutral atomic beam. The beam energy is dependent on the nozzle temperature which can be adjusted for beam energies in the range of 35–90 meV. For diffraction and time-of-flight measurements, a mechanical chopper was used to modulate the beam prior to collision with a duty cycle of 50%. For collection of time-of-flight data, the beam is modulated with a pseudorandom chopping sequence for cross-correlation analysis.[42] Collimation of the beam occurs through a series of apertures, resulting in a 4 mm spot size on the crystal (chopper-to-crystal distance = 0.4996 m) in the UHV scattering chamber (base pressure 3×10^{-10} Torr). The crystal was mounted onto a six-axis manipulator which can be positioned precisely to control the incident angle, θ_i, the azimuth, φ, and the tilt, χ, with respect to the scattering plane. Post-collision, the atoms travel along a 1.0234 m (crystal-ionizer distance) triply differentially pumped rotatable detector arm, with an angular resolution of 0.29° FWHM, after which they are ionized by electron bombardment. The ions then pass through a quadrupole filter where they are mass-selected before being collected by an electron multiplier.

Angular distributions were obtained by scanning the detector at 0.1° computer-controlled increments while holding the incident angle at a fixed value.

The rotational experiments are carried out with n-H_2 or n-D_2 molecular beams, with varied stagnation pressures. The rotational populations of H_2 and D_2 were not measured directly, but instead were calculated based on previous theoretical and experimental results. Generally, the ratio of ortho- to para-$H_2(D_2)$ is determined by the source temperature, and subsequent ortho–para conversion does not occur during the expansion.[43] The occupation of rotational states follows a near Boltzmann distribution within the respective ortho/para families, and can be characterized by an effective rotational temperature, T_R, which can be expressed with an empirical fit[44] for n-D_2 as

$$\log\left(\frac{T_R}{T_0}\right) = -0.40 \, \log\left[P_0 d \times \frac{T_{ref}}{T_0}\right] + 0.16, \qquad (1)$$

where the reference temperature, T_{ref}, is 298 K, T_0 is the beam temperature, and $P_0 d$ is the stagnation pressure times the nozzle diameter, given in units of Torr cm. The beam energies, rotational temperatures, and corresponding rotational populations for the experiments performed herein are given in Table I. In cases where high-translational-energy D_2 beams were created by seeding in a 1:1 mixture of H_2 and D_2, the rotational populations of the D_2 molecules were calculated using the measured nozzle temperature instead of the temperature derived from time-of-flight analysis, allowing for a more precise determination of these data points. All experiments reported herein used incident energies below 120 meV for D_2 such that over 99% of the impinging D_2 molecules are in their vibrational ground states. Additionally, vibrational excitations can be ignored due to the large inter-level spacing for D_2 molecules (~380 meV).[45]

C. Theoretical modeling

Theoretical analysis of the $H_2(D_2)/CH_3$–Si(111) system has been performed within the Born-Oppenheimer static surface approximation (BOSSA). The Born-Oppenheimer approximation is justified by the different time scales associated with the motion of nuclei and electrons. The static surface approximation (SSA) is justified by the mass mismatch between the surface-terminating CH_3 layer and the H_2 and D_2 projectiles (although low recoil effects could be expected). Furthermore, experimental results have been extrapolated to a surface temperature of 0 K via the Debye-Waller correction,

TABLE I. D_2 beam parameters, rotational temperatures, and corresponding rotational populations.

T_0 (K)	E_B (meV)	T_R (K)	n(j = 0)	n(j = 1)	n(j = 2)
184	55.5	46.7	0.654	0.333	0.013
231	69.9	61.3	0.620	0.332	0.047
234	70.6	64.9	0.610	0.332	0.057
289	87.3	68.2	0.598	0.331	0.069
307	105.4	95.5	0.498	0.324	0.168
356	107.3	94.1	0.503	0.325	0.163

which allows a direct comparison between experimental measurements and SSA theoretical results. Working within this framework, a six-dimensional (6D) PES is first computed, and then is included in the nuclear Hamiltonian to perform dynamics simulations.

1. Electronic structure calculations

The 6D PES, for which the degrees of freedom are illustrated in Figure 1, has been computed by interpolation of a density functional theory energy data set. To perform the DFT periodic calculations, the plane-wave-based code VASP (Vienna *ab initio* Simulation Package)[46,47] has been used. In these calculations, the exchange-correlation energy of the electrons has been described using the generalized gradient approximation (GGA); in applying the GGA, the Perdew-Burke-Ernzerhof (PBE) functional[48] has been used. Additionally, the ion cores have been described using the PAW (projector augmented-wave) method.[49]

The $H_2(D_2)/CH_3$–Si(111) system has been modeled using a five-layer slab and a 2×2 hexagonal surface unit cell, as shown in Figure 1. The size of the unit cell has been chosen to mitigate interaction between molecules in adjacent cells, which are present in the calculations due to the use of periodic boundary conditions (PBCs). To avoid artifacts caused by the use of PBC in the z direction, a vacuum layer of 21 Å has been set. A $7 \times 7 \times 1$ Monkhorst-Pack grid of k-points was used to sample the Brillouin zone.[50] The cutoff energy for the plane-wave basis has been set to 650 eV. The lattice bulk parameter has been optimized, finding a value of $a = 5.48$ Å, which agrees well with the known experimental value (5.431 Å).[51] The surface interlayer distances have also been relaxed until the forces were below a 1 meV/Å threshold.

2. Modified Shepard interpolation method

To build the continuous 6D PES, $V_{6D}(x, y, z, r, \Theta, \varphi)$, representing the ground electronic state structure of the $H_2(D_2)/CH_3$–Si(111) system, this work makes use of the modified Shepard (MS) interpolation method, originally developed by Collins *et al.*[52,53] to study gas-phase reactions, and later adapted to study reactive scattering of molecules from surfaces.[54–57] Specifically, a recent implementation of the MS method,[58] which includes strict plane group symmetry and translational periodicity, is utilized herein. In the MS method, the interpolated PES is described by a weighted series of Taylor expansions centered on a number of DFT energy data points, N. These data points are sampled throughout the configuration space of the system. Thus, the global PES at any configuration $\vec{Q}$ is given by

$$\mathrm{V}\left(\vec{Q}\right) = \sum_{i=1}^{N} \sum_{g \in G_{CNP} \times G_{PG}} w_{(g \circ i)}\left(\vec{Q}\right) S_{(g \circ i)}\left(\vec{Q}\right), \quad (2)$$

where w is a weighting function, G_{CNP} and G_{PG} are the molecular permutation and plane symmetry groups, and S is the Taylor series expansion of the PES in the vicinity of the geometry of data point $(g \circ i)$, which denotes that the quantity for data point i has been transformed according to the symmetry operation $g \in G_{CNP} \times G_{PG}$. Note that $\vec{Q}$ in Equation (2) does not represent the set of Cartesian coordinates used to compute the DFT energy points, but a set of redundant internal coordinates relative to them through the Wilson B matrix.[58] The Taylor series expansion used here is expressed as

$$S_i\left(\vec{Q}\right) = E(i) + \Delta E(i)^T \Delta\varsigma(i) + \frac{1}{2}\Delta\varsigma(i)^T F(i)\Delta\varsigma(i), \quad (3)$$

where $E(i)$ is the energy at the data point geometry i, $\Delta E(i)$ is the vector of first derivatives at data point i with respect to elements of $\varsigma(i)$, which are local coordinates resulting from a linear combination of the redundant internal coordinates $\vec{Q}$, $F(i)$ is the matrix of second derivatives at data point i with respect to elements of $\varsigma(i)$, and $\Delta\varsigma(i)$ is the displacement of the point $\vec{Q}$ from the data point geometry $\vec{Q}$ in $\varsigma(i)$ coordinates.

It is important to note that the MS method uses a non-homogeneous sampling of the configuration space, so that more DFT energy points are used in the dynamically relevant regions. These regions are selected by using classical dynamics through a feedback process, hereafter called the GROW process. The first step begins with an initial basic
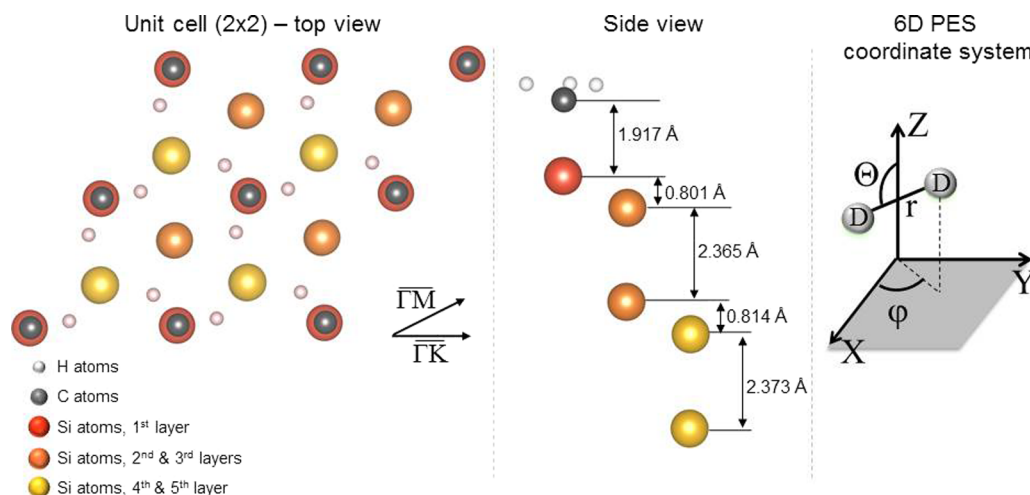

FIG. 1. Schematic representation of the CH_3–Si(111) unit cell used, viewed from above (left panel) and the side (center panel). Right panel shows the degrees of freedom included in the PES.

version of the PES, defined in this case by only 50 DFT energy points. Then a small batch of classical trajectories is run on this basic PES, and from these trajectories new geometries are selected and added to the PES, thereby augmenting it. The new geometries are chosen according to two different criteria:[59] either new energy data points are added to the region most frequently visited by the trajectories or they are added to regions suspected to be the most inaccurate ones. Periodically, a larger batch of trajectories is run and used to compute some observables, which in this case are the rotational excitation probabilities. If the probabilities change significantly with the number of DFT data points added to the PES, the procedure goes back to the second step of running a small batch of trajectories. If the probabilities do not change significantly, the PES is considered converged, as illustrated in Figure 2. At this point, it should be pointed out that in order to properly sample the dynamical regions relevant to this analysis, the incident conditions of the classical trajectories are selected to correspond to the experimental conditions.

3. Quasi-classical dynamics

Quasi-classical dynamics—i.e., classical dynamics including the zero-point energy of the molecule—have been used to both grow and scrutinize the PES. To compute quasi-classical trajectories, the classical equations of motion are solved using the velocity-Verlet algorithm.[60] For each initial energy (E_i) and incident angle (θ_i), the classical scattering probability is calculated as an average over the molecular initial conditions, i.e., over the internal coordinates and conjugated momenta. The initial molecular conditions are sampled using a Monte Carlo method. To ensure low statistical error, approximately 2.5×10^4 trajectories are computed for each set of initial conditions (E_i, θ_i). In these calculations, a molecule is considered reflected (and the integration ends) whenever the final distance between the molecule and the surface, z_f, becomes equal to initial distance, z_i, with the molecular velocity vector pointing towards the vacuum. To analyze rotational excitation upon scattering using classical dynamics, it must be taken into account that the classical angular momentum (L) follows a continuous distribution. Therefore, to analyze rotational excitations, the continuous representation is transformed into a discrete one.[61,62] This
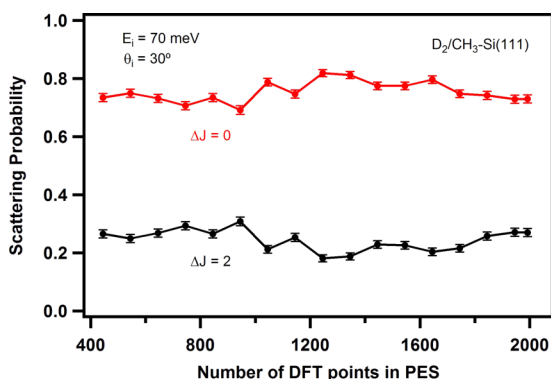
FIG. 2. Elastic and inelastic scattering probabilities as a function of the number of DFT points added to the PES data set.

transformation is performed, in general, by evaluating the closest integer that satisfies

$$j = \frac{1}{2}\left[-1 + \left(1 + \frac{4L^2}{\hbar^2}\right)^{1/2}\right]. \tag{4}$$

However, quantum selection rules for homonuclear diatomic molecules only allow rotational transitions for which $\Delta j = \pm 2$. Therefore, to obtain D_2 rotational excitation probabilities, the initial rotational state of the molecule is considered, and only the closest even or odd integers that satisfy Equation (4) are evaluated.

4. Quantum dynamics

Diffraction probabilities are computed herein by solving the time-dependent Schrödinger (TDS) equation of the nuclear Hamiltonian using the multi-configuration time-dependent Hartree (MCTDH) method[63,64] which has already been successfully used to study diffraction of atomic projectiles,[65] as well as reactive scattering of molecular projectiles.[66–68] In the MCTDH method, the nuclear wavefunction is written as a sum of products of single-particle functions (SPFs). In this particular case, each SPF (χ) combines up to two degrees of freedom, and so the nuclear function of this system can be written as follows:

$$\Phi(Q,t) = \sum_{h=1}^{N_{x,y}} \sum_{k=1}^{N_z} \sum_{l=1}^{N_{\Theta,\varphi}} C_{hkl}(t)\chi_h(x,y;t)$$
$$\times \chi_k(z;t)\chi_l(\Theta,\varphi;t), \tag{5}$$

where Q represents the set of nuclear coordinates, and $(N_{x,y}, N_z, N_{\Theta,\varphi})$ represents the number of SPFs used to describe each mode. The SPFs are in turn represented by linear combinations of time-independent primitive basis functions. In order to reduce the computational effort, and taking advantage of the lack of reactivity of D_2/CH$_3$–Si(111) in the energy range considered here, five-dimensional (5D) calculations have been performed, in which the atom-atom distance has been kept frozen at the equilibrium D_2 gas-phase distance (see Table II for calculation parameters). Within the MCTDH framework, the equations of motion for both the expansion coefficients and the SPFs are derived from the Dirac-Frenkel variational principle which leads to a set of coupled equations. In general, solving this coupled-equation system requires less computational effort than standard time-dependent wave packet propagation (TDWP) methods,[69] because the number of SPFs needed is smaller than the number of time-independent basis functions used in the standard TDWP methods. To obtain elastic and inelastic diffraction probabilities, a flux analysis is carried out with the aid of a complex absorbing potential located in the non-interaction z region.[70]

Finally, it should be noted that to take full advantage of the MCTDH formalism, the multidimensional non-separable PES has to be rewritten as a linear combination of products of one- or two-dimensional functions. This transformation can be performed using the POTFIT algorithm, which is based on the approximation theorem of Schmidt,[71] provided with the Heidelberg MCTDH package. Thus, the multi-dimensional PES is rewritten as follows:

TABLE II. Parameters used in the 5D $(x, y, z, \Theta, \varphi)$ MCTDH calculations.

Initial wave packet	
Width, Δz_0 (Å)	0.9
Position, z_0 (Å)	14.74
Momentum, k_{z_0} (a.u.)	[4.96, 6.61]
Primitive grid parameters	
Type x,y	FFT DVR
x,y-range (Å)	[0, 7.75]
$M_{x,y}$	65
Type z	FFT DVR
z-range (Å)	[−2.66, 15.33]
M_z	200
Type Θ, φ	Legendre DVR
$M_{\Theta\varphi}$	20×17
SPF basis	
$N_{x,y}$	65
N_z	17
$N_{\Theta,\varphi}$	17
Complex absorbing potential	
z-range (Å)	[5.62, 15.33]
Strength (a.u.)	6×10^{-4}

$$V(Q) \approx V_{approx} = \sum_{j=1}^{m_{x,y}} \sum_{k=1}^{m_{zr}} \sum_{l=1}^{m_{\Theta,\varphi}} c_{jkl} \zeta_j^{(x,y)}$$
$$\times (x, y) \, \zeta_k^{(z)} (z) \, \zeta_l^{(\Theta,\varphi)} (\Theta, \varphi), \quad (6)$$

where $\zeta_j^{(u)}$ is the jth one- or two-dimensional function used to describe the single particle mode u (the so-called natural potential). These functions are the ones used to expand the SPFs, which are represented in a primitive grid of points. The expansion coefficients c_{jkl} are determined by the overlap between the multi-dimensional PES and the natural potentials (see Table III for representative parameters for PES refits).

TABLE III. Parameters used to represent the PES in a suitable form for the MCTDH equations of motion using POTFIT. Δ_{rms}^{rw}, Δ_{rms}^{w} represent the root-mean-square error on all grid points and on relevant grid points, respectively. $\max(\varepsilon^r)$, $\max(\varepsilon)$ represent the maximum error on all grid points and on relevant grid points, respectively.

Natural potential basis	
m_z	20
$m_{x,y}$	Contr.
$m_{\theta,\varphi}$	20
Relevant region of the fit	
z (Å)	> -0.66
V (eV)	<3
r (Å)	0.767
V_{max} (eV)	20
POTFIT accuracy	
N_{iter}	3
Δ_{rms}^{rw}, Δ_{rms}^{w} (meV)	3.1, 4.4
$\max(\varepsilon^r)$, $\max(\varepsilon)$ (meV)	150, 226

III. RESULTS AND DISCUSSION

A. H_2 and D_2 diffraction from CH_3–Si(111)

Angular distributions of H_2 scattered from CH_3–Si(111) are shown in Figure 3 along the high-symmetry $\langle \bar{1}2\bar{1} \rangle$ $(\bar{\Gamma} - \bar{M})$ and $\langle 01\bar{1} \rangle$ $(\bar{\Gamma} - \bar{K})$ azimuthal alignments; both diffraction spectra were taken under identical conditions, with a room temperature beam ($E_i = 81.4$ meV) and cold surface temperature ($T_s = 140$ K). The zeroth-order specular ($\theta_i = \theta_f$) diffraction peak and elastic first-order diffraction peaks are clearly resolved here; the relatively large first-order diffraction peak intensities compared to specular indicate a significant corrugation of the gas-surface potential. Elastic diffraction peaks arise when the kinematic condition for Bragg diffraction for in-plane scattering is satisfied such that

$$\Delta \vec{K} = \vec{k}_i (\sin \theta_f - \sin \theta_i) = \vec{G}_{mn}, \quad (7)$$

where $\Delta \vec{K}$ is the change in the surface-parallel component of the H_2 wavevector $\vec{k}_i$, θ_i and θ_f are the initial and final scattering angles relative to the surface normal, and $\vec{G}_{mn}$ is the surface reciprocal lattice vector. Information on the surface geometry and lattice constant can be determined by analyzing the spacing between diffraction peaks; the spacings between specular ($\Delta \vec{K} = 0$) and first-order diffraction peaks are $\Delta \vec{K} = 1.90$ Å^{-1} and 3.29 Å^{-1} along $\langle \bar{1}2\bar{1} \rangle$ and $\langle 01\bar{1} \rangle$, respectively, corresponding to a hexagonally packed methyl adlayer with a real-space lattice constant of 3.82 Å. This value is in excellent agreement with previous helium diffraction measurements from this methyl-terminated Si(111) surface,[13] with both identifying a (1×1) commensurate monolayer of methyl groups on Si(111).

Unlike with helium diffraction, when a H_2 or D_2 molecule scatters from the surface, it is capable of exchanging energy between its internal rotational and translational degrees of freedom; this exchange must still conserve total energy such that

$$E_f - E_i = \frac{\hbar^2 k_f^2}{2m} - \frac{\hbar^2 k_i^2}{2m} = \Delta E_{int}^{rot}. \quad (8)$$

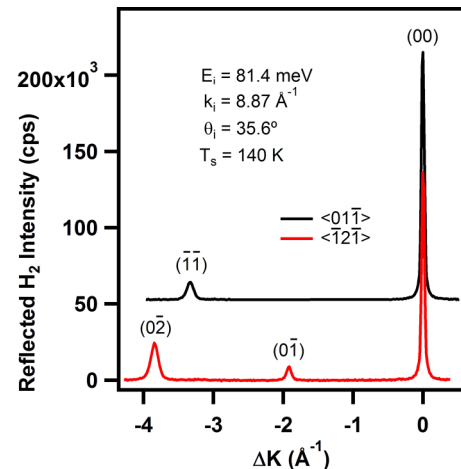FIG. 3. Representative diffraction spectra for H_2 on CH_3–Si(111) along two principal symmetry axes, $\langle 01\bar{1} \rangle$ (black) and $\langle \bar{1}2\bar{1} \rangle$ (red), as a function of parallel momentum exchange.

Here, $\hbar$ is the reduced Planck constant, m is the mass of H_2 or D_2, E_i and E_f are the initial and final kinetic energies of the projectile, respectively, and ΔE_{int}^{rot} is the energy exchanged between rotational and translational modes, which equals a difference between the molecule's rotational energy levels as determined by the rigid rotor model; note that symmetry constraints within the hydrogen molecule impose a rotational selection rule of $\Delta j = \pm 2$. This phenomenon of internal energy exchange results in RID peaks scattered at distinct angles from their parent elastic diffraction peaks such that

$$\theta_f^{RID} = \arcsin\left[\frac{k_i \sin\theta_i - \vec{G}_{mn}}{\left(k_i^2 - \frac{2m}{\hbar^2}\Delta E_{int}^{rot}\right)^{1/2}}\right]. \quad (9)$$

Figure 4(a) shows a diffraction spectrum for H_2 scattering from CH_3–Si(111), which includes a small peak associated with the specular $j = 0 \rightarrow 2$ rotational excitation; note that RID peaks are labeled using the (j_i, j_f, m, n) notation, whereas elastic diffraction peaks are labeled with the (mn) notation. By positioning the rotatable detector arm at the final scattering
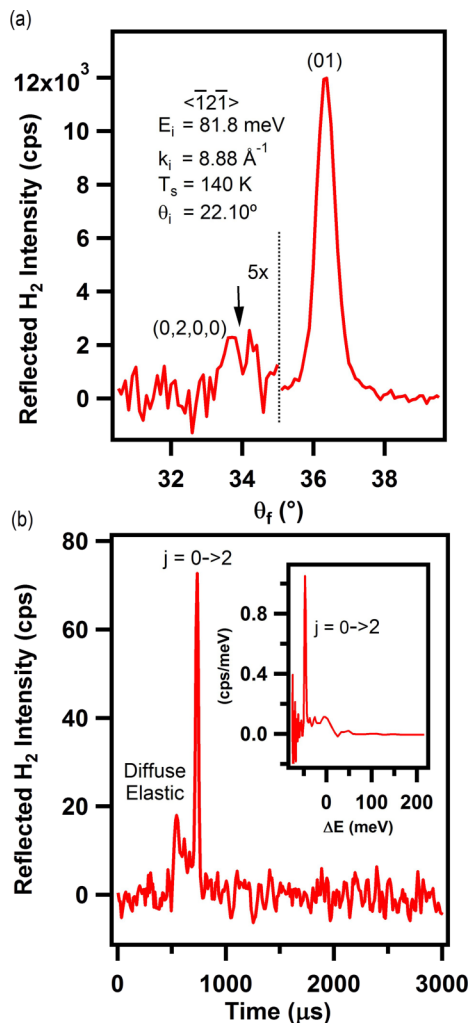

FIG. 4. (a) Background-subtracted H_2 diffraction spectrum with magnified feature attributed to (0,2,0,0) rotationally inelastic diffraction; (b) corresponding time-of-flight spectrum and energy-exchange spectrum (inset) measured at position indicated by the arrow in (a), demonstrating $j = 0 \rightarrow 2$ inelastic transition.

angle of this RID peak, time-of-flight measurements can be used to confirm the inelastic scattering of the hydrogen molecules. A cross-correlation time-of-flight spectrum taken at the same conditions as this peak is shown in Figure 4(b); a diffuse elastic and rotationally inelastic hydrogen peak are observed to be fully resolved from one another. The flight time separation between the elastic and inelastic peaks can be used to calculate the energy exchange as a result of inelastic scattering from the surface (Figure 4(b), inset). The RID peak shown in Figure 4(b) arrived at a longer time than the elastic peak, indicating a loss in energy and velocity of the H_2 molecules; specifically, the calculated energy agrees well with the expected value of 45.4 meV for a $j = 0 \rightarrow 2$ rotational excitation for an incident H_2 molecule.

In order to obtain highly resolved elastic and inelastic diffraction peaks in this range of relatively low beam energies, the surface probe was switched from H_2 to D_2. The predominant advantage in using D_2 is that the energy required to transition between rotational states is half that of H_2 (D_2: $j = 0 \rightarrow 2$, 22.7 meV), as predicted by the rigid rotor model, leading to a greater probability of rotational excitation. In addition, the combination of nuclear spin states for each of the nuclei in H_2 and D_2 leads to the formation of ortho (symmetric) and para (antisymmetric) spin isomers, which pair with a set of rotational states to maintain the antisymmetry of the molecule as a whole. The degeneracy of these spin states causes only ~25% of n-H_2 molecules to be in the $j = 0$ state, whereas ~66% of n-D_2 molecules are in the rotational ground state.

The utility of D_2 as a surface probe is demonstrated in Figure 5(a), in which a diffraction spectrum for a room temperature D_2 beam from CH_3–Si(111) shows several high-intensity elastic and RID peaks. The resolution of inelastic peaks in D_2 spectra allows for precise measurements of rotationally inelastic transition probabilities; specifically, the rotational excitations can be measured as a function of scattering angle or beam energy, as seen in Figure 5(b).

As the setup of this instrument does not allow for direct measurement of the absolute incident beam flux, the probabilities of rotationally inelastic diffraction are evaluated as ratios of inelastic to elastic diffraction intensities.[26,28,32] This ratio enables the number density measured by the detector to be effectively converted into flux by accounting for the change in beam velocity that results from transferring energy between translational and rotational degrees of freedom. In addition, this approach obtains accurate values by accounting for the influences of instrumental broadening, finite crystal temperature, energy spread of the beam, and the initial rotational distributions of the incident beam.

Specifically, to relate a RID peak to its parent elastic peak, the following expression is used:

$$r(j_i, j_f, m, n) = \frac{I(j_i, j_f, m, n)}{I(mn)\,n(j_i)}\sqrt{\frac{E_i + \Delta E_{rot}}{E_i}}$$
$$\times \exp\left[2W_{j_i, j_f, m, n} - 2W_{mn}\right]. \quad (10)$$

In this expression, $I(j_i, j_f, m, n)$ and $I(mn)$ are the peak area integrated intensities of D_2 molecules scattered from
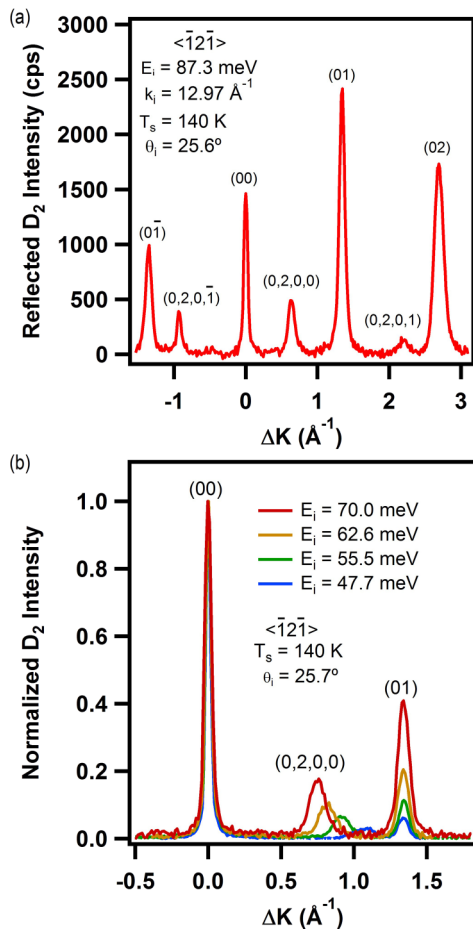
FIG. 5. (a) Representative diffraction spectrum for D_2 on CH_3–Si(111), featuring high-intensity elastic and rotationally inelastic diffraction peaks; (b) D_2 diffraction spectra normalized to specular intensity demonstrate the effect of incident energy on the location of RID peak, as well as relative intensity of RID and elastic diffraction peaks (number density, not yet flux corrected).

a crystal of finite surface temperature T_s. The square root term corrects for the velocity difference between elastic and rotationally inelastic scattering events, as discussed above.[28] Additionally, the rotational distributions of the impinging atoms are accounted for with $n(j_i)$. By using this ratio rather than a pure probability, the effects of surface defects and beam geometry are eliminated and experimental error associated with evaluation of the Debye-Waller factor, $W(T_s)$, is mitigated.

Attenuation of diffraction intensity due to thermal motion at the CH_3–Si(111) surface is accounted for via the Debye-Waller factor, which can be approximated in the semi-classical limit of a quantum-mechanical description of inelastic scattering as

$$W(T_s) = \frac{12m \left[E_i \cos^2\theta_i + D \right] T_s}{M_{eff} k_B \Theta_D^2},$$ (11)

for the specular peak, where D is the attractive well depth for a gas-surface interaction potential, M_{eff} is the effective surface mass that a given H_2 or D_2 molecule interacts with (assumed here to be 15 amu), k_B is Boltzmann's constant, and Θ_D is the surface Debye temperature.[43,72] The attenuated intensities of RID peaks are corrected using the Debye-Waller

factor associated with their parent diffraction peaks, which is a reasonable assumption based on the small parallel momentum transfer associated with the (0,2,0,0) and (0,2,0,$\bar{1}$) peaks.[61,73]

The Debye-Waller factor can be quantified by relating the intensity of a peak to its ideal intensity for a lattice at 0 K, I_0, such that

$$I = I_0 e^{-2W(T_s)}.$$ (12)

As such, the natural log of I/I_0 *versus* T_s produces a linear decay, from which the Debye-Waller factor for a given system can be extracted. Figure 6(a) shows the thermal attenuation of the specular peak at a given set of incident conditions over surface temperatures ranging from 140 to 350 K; the inset of this figure exhibits the linear decay which provides the Debye-Waller factor for the H_2/CH_3–Si(111) system. This exponential factor is derived from the normal and parallel momentum transfers during the scattering process (Δk_z and ΔK, respectively) and the associated mean-square
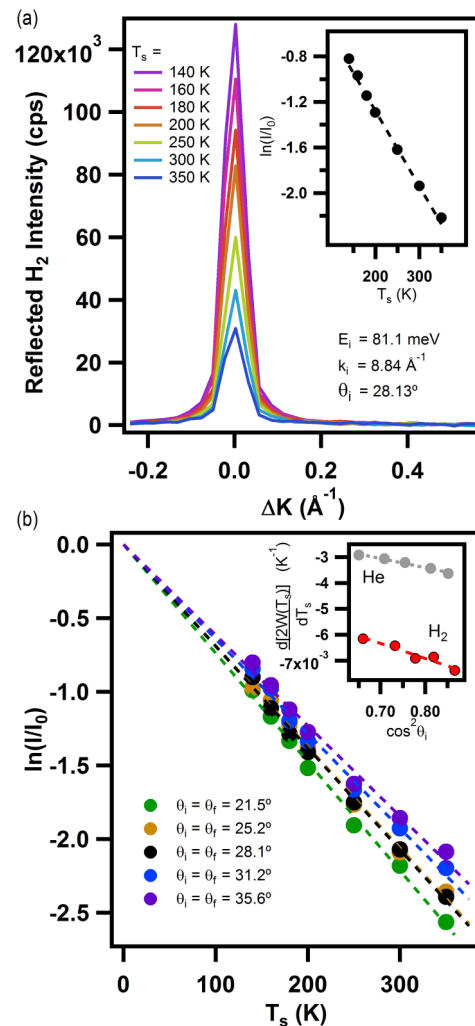

FIG. 6. (a) Decay of specular ($\theta_i = \theta_f$) peak intensity as a function of CH_3–Si(111) surface temperature, plotted vs. parallel momentum exchange; natural log of intensity decay vs. sample temperature (inset) confirms application of Debye-Waller formalism. (b) Intensity decays for five incident angles (including that of panel (a)), with the slopes of these decays plotted against the square of the cosine of the incident angle (inset), as compared to the same conditions for He diffraction.

displacements (MSD) of the crystal atoms ($\langle u_z^2 \rangle$ and $\langle u_\parallel^2 \rangle$) such that

$$2W(T_s) = \Delta k_z^2 \langle u_z^2 \rangle + \Delta K^2 \langle u_\parallel^2 \rangle. \qquad (13)$$

For the specular peak,

$$\Delta \vec{k_z} = 2\vec{k_i} \left[\left(\cos^2\theta_i + \frac{D}{E_i} \right)^{1/2} \right]. \qquad (14)$$

The perpendicular MSD and the well depth (D) of the gas-surface interaction potential can therefore be determined by plotting the derivative $d2W(T_s)/dT_s$ *versus* $\cos^2\theta_i$ and extracting the slope and y-intercept, respectively.[13,74] Figure 6(b) shows diffraction decay rates at several angles, and the inset demonstrates the angular dependence of the Debye-Waller factor that provides a perpendicular MSD of $(1.85 \pm 0.30) \times 10^{-5}$ Å^2 K^{-1}. Analogous data for the He/CH$_3$–Si(111) system are also shown in this figure, and its comparable slope provides a perpendicular MSD of $(1.0 \pm 0.1) \times 10^{-5}$ Å^2 K^{-1}, just slightly below what is measured for the H$_2$ system.[13] The difference in y-intercepts indicates a higher potential well depth for H$_2$ ($D = 32 \pm 9$ meV) than for He ($D = 7.5 \pm 2.6$ meV), as expected based on the higher degree of polarizability for H$_2$. Equation (11) uses these well depths to provide a surface Debye temperature of 723 K (503 cm^{-1}) for the H$_2$ system, which is considerably lower than 983 K (683 cm^{-1}) measured via He diffraction. While the surface Debye temperature measured for H$_2$/CH$_3$–Si(111) differs from He, both molecules seem to interact with a vibrational mode of the methyl adlayer: either Si–C bending (507 cm^{-1}) or Si–C stretching (683 cm^{-1}).[75]

Figure 7 shows plots of r(0,2,0,0) and r(0,2,0,$\bar{1}$) for D$_2$ on CH$_3$–Si(111) as a function of beam energy, as calculated via Equation (10) with Debye-Waller corrections. There is

a clear increase in rotational excitation probability with increasing beam energy, which is expected due to higher-energy incident molecules penetrating further into the surface charge density, thereby increasing the corrugation of the gas-surface interaction potential and the resultant torque on the non-spherical molecule. The dependence of rotational excitation probability on incident angle is weaker, with a more normal incident angle eliciting slightly more rotational probability for the first-order RID peak, and no apparent trend in angular dependence for the specular RID peak.

B. Theoretical analysis

Quantum and classical dynamics simulations have been carried out with the goal of more accurately interpreting experimental measurements. First, to assess the accuracy of the theoretical tools employed herein, in particular the interpolated PES, quantum dynamics simulations have been compared with experimental measurements obtained at several representative sets of initial conditions (Figure 8). To perform this comparison, the quantum simulations consider the initial rotational distribution of the molecular beam (Table I). Overall, a good agreement is observed between both sets of data; in particular, the theoretical and experimental spectra exhibit an increase in the rotational excitation probability as the incident energy increases. These results indicate that the calculated PES is accurate enough to perform the required analysis.

In Figure 7, quantum ratios r(0,2,0,0) and r(0,2,0,$\bar{1}$) (dashed lines) are compared with the experimental ones; it should be noted that theoretical probabilities for a fixed incident energy were within 1° of the experimental scattering angle. The theoretical results generally agree with the increase
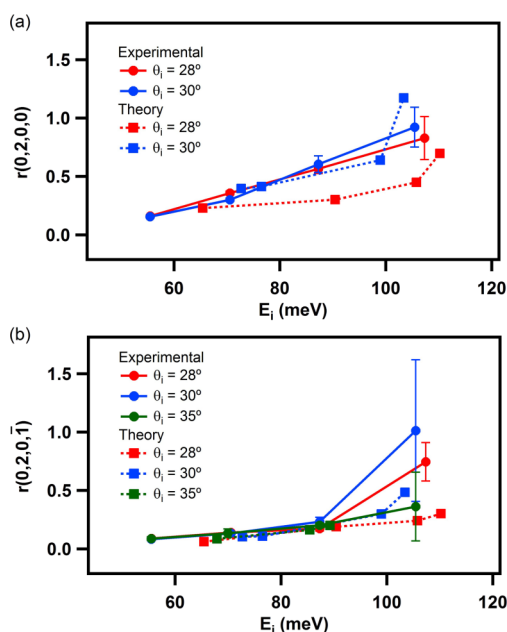

FIG. 7. Rotational probabilities for the $j = 0 \rightarrow 2$ transition for experimental (solid) and theoretical (dashed) data as a function of beam energy and incident angle for (a) specular and (b) first-order diffraction peaks.
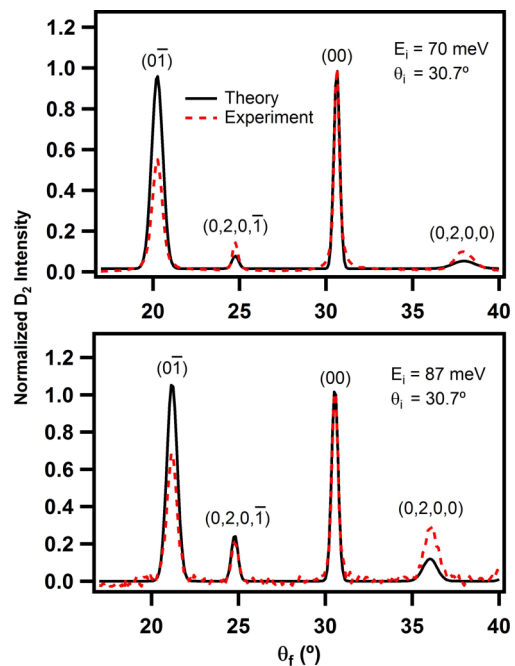

FIG. 8. Comparison of experimental (red dashed line) and simulated diffraction spectra (black solid line) for two representative sets of incident conditions.

in rotational excitation probability as a function of incident energy. Slight disagreement between theory and experiment is observed at higher beam energies, which is likely due to the strong corrugation of this system, as well as the use of a frozen-surface model for the PES, which becomes a less reasonable approximation when the energy of incident D_2 molecules nears the rotational barrier of the methyl group (~100 meV for a surface temperature of 0 K).[14]

Having established the accuracy of the PES, a quasi-classical dynamics analysis can be performed on the regions of the PES that determine the characteristics of the diffraction spectra. To establish the validity of the classical analysis, quantum and classical total elastic and rotational excitation probabilities have been compared. Figure 9 displays the elastic and rotational excitation probabilities for H_2 (classical results only) and D_2 (quantum and classical results) as a function of the beam energy, along the $\bar{\Gamma} - \bar{M}$ direction, for three different incident angles. Several notable features are evident in this figure: (a) in the case of H_2, rotational excitation stays below 5% over the entire energy range investigated; (b) for D_2, quantum and classical simulations yield rather similar results—the classical rotational excitation probability fluctuates around 20%-25%, whereas the quantum probability is slightly higher (30%-35%). These results agree with the experimental results reported above, which show the presence of large RID in the diffraction spectra of D_2, whereas negligible RID has been observed for H_2 in diffraction spectra. This qualitative agreement between classical and quantum rotational excitation probabilities justifies further analysis of the systems using classical trajectories calculations, especially

for incidence energies below 90 meV, beyond which point classic and quantum rotational excitation probabilities begin exhibiting different trends.

Classical trajectories have revealed that most molecules are scattered at a classical turning point around 2 Å from the plane formed by the H atoms in the methyl groups, with a molecular bond length around 0.78 Å. Given that these values are almost independent of θ_i and E_i within the range of experimental incident conditions, the characteristics of the potential have been analyzed at these (z, r) values. Figure 10 illustrates the one-dimensional (1D) potential energy profile along both the $(\bar{\Gamma} - \bar{M})$ and $(\bar{\Gamma} - \bar{K})$ azimuthal directions. One important feature of the PES that can be observed in Figure 10 is that the corrugation of the potential due to H atoms is very small compared to that due to C atoms, as the only indication of the presence of H atoms is the small shoulder seen between the hill and the valley. Another interesting feature that can be extracted is that the projectiles are guided towards the hollow and bridge sites. It is clear that molecules with incident energies below 90 meV cannot adiabatically approach the top site or surrounding sites; therefore most of the molecules are scattered from the hollow and bridge sites. This behavior is also corroborated by analysis of classical trajectories, which indicates that the molecules are scattered far from the top site after being efficiently steered towards the hollow and bridge sites.

Finally, Figure 10 also reveals a marked anisotropy of the potential in the classical turning point regions. For a closer inspection of the potential anisotropy, Figure 11 displays the relative potential energy as a function of the molecular orientation angle, Θ, at several z-distances from the surface. The anisotropy of the potential is observed to increase rapidly when the molecule approaches the surface, except in the case of the top site, which molecules do not sample, as discussed above. This rapid increase in the corrugation around the classical turning points is responsible for the substantial rotational excitation found in this system. It is noted that insubstantial differences are obtained for the trajectories followed by H_2 and D_2 molecules, when similar incident molecular velocities are considered. It can thus be concluded that the anisotropy experienced by both isotopes is similar, and therefore that the different rotational excitation observed
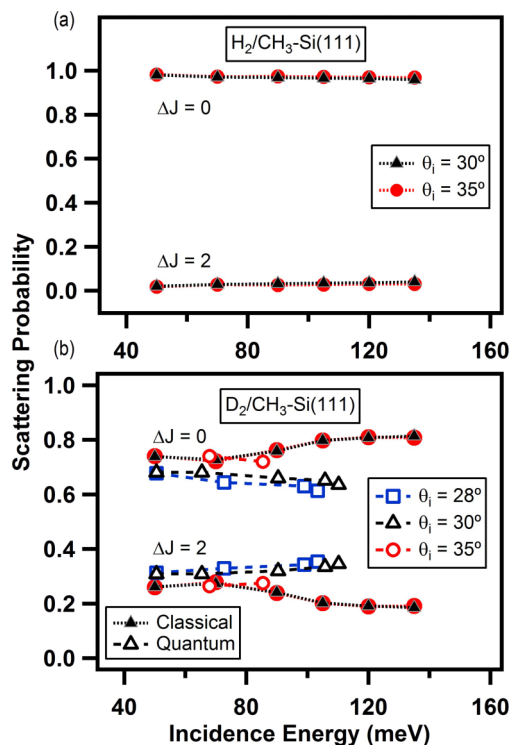
FIG. 9. Quantum (open symbols) and classical (solid symbols) elastic ($\Delta J = 0$) and rotational excitation ($\Delta J = 2$) probabilities as a function of the incident energy along the $\bar{\Gamma} - \bar{M}$ azimuthal direction, for several incidence angles.
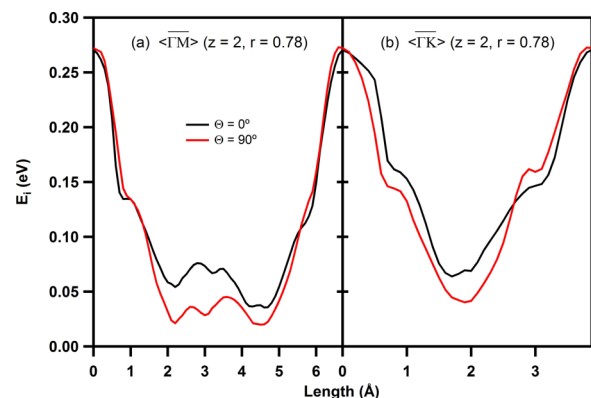
FIG. 10. 1D potential energy surfaces along the high-symmetry directions $\bar{\Gamma} - \bar{K}$ and $\bar{\Gamma} - \bar{M}$, with $z = 2$ Å and $r = 0.78$ Å, for molecules approaching with surface-parallel ($\Theta = 90°$, red lines) and perpendicular ($\Theta = 0°$, black lines) orientations (cf. Figure 1).
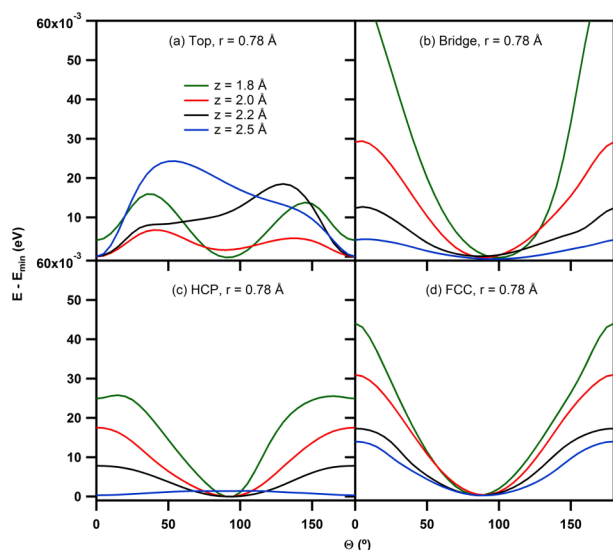
FIG. 11. Relative 1D potential energy surfaces as a function of molecular orientation angle (Θ) for four high-symmetry sites at several z values ($r = 0.78$ Å); E_{min} represents the energy of the system when H_2 is in its equilibrium configuration far from the surface.

is only due to the differences in rotational level spacing ($\sim$45 meV for H_2, $\sim$22 meV for D_2).

Further insight into the nature of the PES can be extracted from Figure 12, which shows a series of *xy*-cuts for several
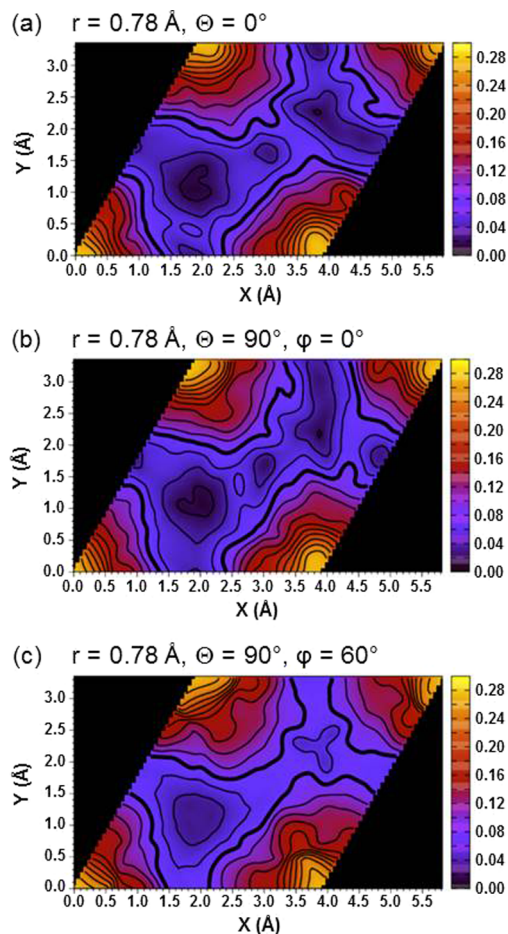
FIG. 12. *xy*-cuts of the potential energy surface with $z = 2$ Å. Bold line corresponds to 0.08 eV, and the spacing between the contour levels is 0.02 eV.

(Θ, φ) orientations. In these plots, z and r values have been chosen according to the average values at the classical turning points revealed by a classical trajectory analysis, as discussed above. This figure indicates strong corrugation in the PES and shows that the molecular projectile feels, although rather weakly, the H atoms that belong to the CH_3 groups.

IV. CONCLUSIONS

The diffraction of H_2 and D_2 molecular beams from CH_3–Si(111) was complemented by electronic structure and scattering calculations to investigate the nature of the interaction potential and surface charge density for a technologically relevant organic-functionalized semiconductor interface. Time-of-flight measurements confirmed the presence of rotationally inelastic diffraction for both H_2 and D_2 on this surface, and diffraction measurements demonstrated a stronger probability of rotational excitation for D_2 as compared with H_2, as expected based on the lower energy required for an internal exchange of rotational energy. The probabilities of these $j = 0 \rightarrow 2$ rotational transitions were quantitatively evaluated as a function of beam energy and scattering angle, accounting for the thermal attenuation caused by incoherent motion at the CH_3–Si(111) surface by implementing the Debye-Waller model. The interaction potential between H_2 (D_2) and the surface charge density was then examined via the combination of these experimental results and quantum and quasi-classical dynamics simulations carried out on a continuous potential energy surface for $H_2(D_2)/CH_3$–Si(111) constructed by interpolation of density functional theory energies. Both experimental and theoretical data show high rotational excitation probabilities that increase with incident energy and which are weakly dependent upon incident angle, for the angle range investigated here. Additionally, dynamics calculations have identified the classical turning point regions (2 Å over hollow and bridge sites), and close scrutiny of these regions reveals a large anisotropy in the potential as a function of molecular orientation, which increases rapidly when the molecule approaches these regions and is responsible for the large rotational excitation observed experimentally. Overall, this work has revealed important details regarding the interaction of molecular hydrogen with a model hydrocarbon-decorated interface, which are important for fuel cells and next-generation energy systems.

[1] A. Bansal and N. S. Lewis, J. Phys. Chem. B **102**, 1067 (1998).

[2] A. Bansal, X. Li, I. Lauermann, N. S. Lewis, S. I. Yi, and W. H. Weinberg, J. Am. Chem. Soc. **118**, 7225 (1996).

[3] S. Maldonado, K. E. Plass, D. Knapp, and N. S. Lewis, J. Phys. Chem. C **111**, 17690 (2007).

[4] S. Maldonado and N. S. Lewis, J. Electrochem. Soc. **156**, H123 (2009).

[5] K. E. Plass, X. Liu, B. S. Brunschwig, and N. S. Lewis, Chem. Mater. **20**, 2228 (2008).

[6] L. J. Webb and N. S. Lewis, J. Phys. Chem. B **107**, 5404 (2003).

[7] K. T. Wong and N. S. Lewis, Acc. Chem. Res. **47**, 3037 (2014).

[8] D. Farías, R. Miranda, and K. H. Rieder, J. Chem. Phys. **117**, 2255 (2002).

[9] D. A. King and M. G. Wells, Surf. Sci. **29**, 454 (1972).

[10] D. Farías and R. Miranda, Prog. Surf. Sci. **86**, 222 (2011).

[11] D. Farías, H. F. Busnengo, and F. Martín, J. Phys.: Condens. Matter **19**, 305003 (2007).

[12] D. Barredo, G. Laurent, P. Nieto, D. Farías, and R. Miranda, J. Chem. Phys. **133**, 124702 (2010).

[13] J. S. Becker, R. D. Brown, E. Johansson, N. S. Lewis, and S. J. Sibener, J. Chem. Phys. **133**, 104705 (2010).

[14] R. D. Brown, Z. M. Hund, D. Campi, L. E. O'Leary, N. S. Lewis, M. Bernasconi, G. Benedek, and S. J. Sibener, J. Chem. Phys. **141**, 024702 (2014).

[15] R. D. Brown, Z. M. Hund, D. Campi, L. E. O'Leary, N. S. Lewis, M. Bernasconi, G. Benedek, and S. J. Sibener, Phys. Rev. Lett. **110**, 156102 (2013).

[16] H. Yu, L. J. Webb, J. R. Heath, and N. S. Lewis, Appl. Phys. Lett. **88**, 252111 (2006).

[17] H. Yu, L. J. Webb, R. S. Ries, S. D. Solares, W. A. Goddard, J. R. Heath, and N. S. Lewis, J. Phys. Chem. B **109**, 671 (2005).

[18] R. Hunger, R. Fritsche, B. Jaeckel, W. Jaegermann, L. J. Webb, and N. S. Lewis, Phys. Rev. B **72**, 045317 (2005).

[19] A. Bansal, X. Li, S. I. Yi, W. H. Weinberg, and N. S. Lewis, J. Phys. Chem. B **105**, 10266 (2001).

[20] L. E. O'Leary, E. Johansson, B. S. Brunschwig, and N. S. Lewis, J. Phys. Chem. B **114**, 14298 (2010).

[21] L. J. Webb, S. Rivillon, D. J. Michalak, Y. J. Chabal, and N. S. Lewis, J. Phys. Chem. B **110**, 7349 (2006).

[22] G. Laurent, D. Barredo, D. Farías, R. Miranda, C. Díaz, P. Rivière, M. F. Somers, and F. Martín, Phys. Chem. Chem. Phys. **12**, 14501 (2010).

[23] R. Valero, G.-J. Kroes, Y. Ekinci, and J. P. Toennies, J. Chem. Phys. **124**, 234707 (2006).

[24] D. Farías, R. Miranda, K. H. Rieder, W. A. Diño, K. Fukutani, T. Okano, H. Kasai, and A. Okiji, Chem. Phys. Lett. **359**, 127 (2002).

[25] M. F. Bertino, A. P. Graham, L. Y. Rusin, and J. P. Toennies, J. Chem. Phys. **109**, 8036 (1998).

[26] M. F. Bertino, F. Hofmann, and J. P. Toennies, J. Chem. Phys. **106**, 4327 (1997).

[27] C. Yu, K. B. Whaley, C. S. Hogg, and S. J. Sibener, J. Chem. Phys. **83**, 4217 (1985).

[28] Y. Ekinci and J. P. Toennies, Phys. Rev. B **72**, 205430 (2005).

[29] D. Cvetko, A. Morgante, A. Santaniello, and F. Tommasini, J. Chem. Phys. **104**, 7778 (1996).

[30] P. Rivière, H. F. Busnengo, and F. Martín, J. Chem. Phys. **123**, 074705 (2005).

[31] P. Rivière, M. F. Somers, G. J. Kroes, and F. Martín, Phys. Rev. B: Condens. Matter Mater. Phys. **73**, 205417 (2006).

[32] K. B. Whaley, C. Yu, C. S. Hogg, J. C. Light, and S. J. Sibener, J. Chem. Phys. **83**, 4235 (1985).

[33] P. Nieto, E. Pijper, D. Barredo, G. Laurent, R. A. Olsen, E.-J. Baerends, G.-J. Kroes, and D. Farías, Science **312**, 86 (2006).

[34] P. Nieto, D. Farías, R. Miranda, M. Luppi, E. J. Baerends, M. F. Somers, M. J. T. C. van der Niet, R. A. Olsen, and G.-J. Kroes, Phys. Chem. Chem. Phys. **13**, 8583 (2011).

[35] C. Díaz, F. Martín, G.-J. Kroes, M. Minniti, D. Farías, and R. Miranda, J. Phys. Chem. C **116**, 13671 (2012).

[36] C. Díaz, H. F. Busnengo, P. Rivière, D. Farías, P. Nieto, M. F. Somers, G. J. Kroes, A. Salin, and F. Martín, J. Chem. Phys. **122**, 154706 (2005).

[37] G.-J. Kroes and M. F. Somers, J. Theor. Comput. Chem. **4**, 493 (2005).

[38] G.-J. Kroes and C. Díaz, Chem. Soc. Rev. **45**, 3658 (2015).

[39] N. T. Plymale, Y.-G. Kim, M. P. Soriaga, B. S. Brunschwig, and N. S. Lewis, J. Phys. Chem. C **119**, 19487 (2015).

[40] G. S. Higashi, Y. J. Chabal, G. W. Trucks, and K. Raghavachari, Appl. Phys. Lett. **56**, 656 (1990).

[41] B. Gans, P. A. Knipp, D. D. Koleske, and S. J. Sibener, Surf. Sci. **264**, 81 (1992).

[42] D. D. Koleske and S. J. Sibener, Rev. Sci. Instrum. **63**, 3852 (1992).

[43] G. Scoles, *Atomic and Molecular Beam Methods* (Oxford University Press, New York, 1992), Vol. 2.

[44] M. Faubel, F. A. Gianturco, F. Ragnetti, L. Y. Rusin, F. Sondermann, U. Tappe, and J. P. Toennies, J. Chem. Phys. **101**, 8800 (1994).

[45] D. M. Bishop and R. W. Wetmore, Mol. Phys. **26**, 145 (1973).

[46] G. Kresse and J. Furthmuller, Phys. Rev. B **54**, 11169 (1996).

[47] G. Kresse and J. Hafner, Phys. Rev. B **47**, 558 (1993).

[48] J. P. Perdew, K. Burke, and M. Ernzerhof, Phys. Rev. Lett. **77**, 3865 (1996).

[49] P. E. Blöchl, Phys. Rev. B **50**, 17953 (1994).

[50] H. J. Monkhorst and J. D. Pack, Phys. Rev. B **13**, 5188 (1976).

[51] T. Hom, W. Kiszenik, and B. Post, J. Appl. Crystallogr. **8**, 457 (1975).

[52] J. Ischtwan and M. A. Collins, J. Chem. Phys. **100**, 8080 (1994).

[53] R. P. A. Bettens and M. A. Collins, J. Chem. Phys. **111**, 816 (1999).

[54] C. Crespos, M. A. Collins, E. Pijper, and G.-J. Kroes, J. Chem. Phys. **120**, 2392 (2004).

[55] C. Díaz, J. K. Vincent, G. P. Krishnamohan, R. A. Olsen, G.-J. Kroes, K. Honkala, and J. K. Nørskov, Phys. Rev. Lett. **96**, 1 (2006).

[56] C. Díaz, J. K. Vincent, G. P. Krishnamohan, R. A. Olsen, G.-J. Kroes, K. Honkala, and J. K. Norskov, J. Chem. Phys. **125**, 114706 (2006).

[57] C. Díaz, R. A. Olsen, H. F. Busnengo, and G.-J. Kroes, J. Phys. Chem. C **114**, 11192 (2010).

[58] T. J. Frankcombe, M. A. Collins, and D. H. Zhang, J. Chem. Phys. **137**, 1 (2012).

[59] M. A. Collins, Theor. Chem. Acc. **108**, 313 (2002).

[60] W. C. Swope, H. C. Andersen, P. H. Berens, and K. R. Wilson, J. Chem. Phys. **76**, 637 (1982).

[61] H. F. Busnengo, W. Dong, P. Sautet, and A. Salin, Phys. Rev. Lett. **87**, 127601 (2001).

[62] C. Díaz, H. F. Busnengo, F. Martin, and A. Salin, J. Chem. Phys. **118**, 2886 (2003).

[63] M. H. Beck, A. Jäckle, G. A. Worth, and H.-D. Meyer, Phys. Rep. **324**, 1 (2000).

[64] G. A. Worth, M. H. Beck, A. Jackle, and H.-D. Meyer, The MCTDH Package, version 3.4, 2007, http://mctdh.uni-hd.de/.

[65] M. del Cueto, A. S. Muzas, G. Füchsel, F. Gatti, F. Martín, and C. Díaz, Phys. Rev. B **93**, 060301 (2016).

[66] R. Van Harrevelt and U. Manthe, J. Chem. Phys. **121**, 3829 (2004).

[67] C. Crespos, H. D. Meyer, R. C. Mowrey, and G.-J. Kroes, J. Chem. Phys. **124**, 074706 (2006).

[68] G. P. Krishnamohan, R. A. Olsen, G.-J. Kroes, F. Gatti, and S. Woittequand, J. Chem. Phys. **133**, 144308 (2010).

[69] G.-J. Kroes, Prog. Surf. Sci. **60**, 1 (1999).

[70] D. Neuhauser, Chem. Phys. Lett. **200**, 173 (1992).

[71] A. Jäckle and H.-D. Meyer, J. Chem. Phys. **104**, 7974 (1996).

[72] J. L. Beeby, J. Phys. C **4**, L359 (1971).

[73] B. Gumhalter, Phys. Rep. **351**, 1 (2001).

[74] Z. M. Hund, K. J. Nihill, D. Campi, K. T. Wong, N. S. Lewis, M. Bernasconi, G. Benedek, and S. J. Sibener, J. Chem. Phys. **143**, 124705 (2015).

[75] T. Yamada, M. Kawai, A. Wawro, S. Suto, and A. Kasuya, J. Chem. Phys. **121**, 10660 (2004).